01 Feb 2013

Pore Geometry Effects on Intrapore Viscous to Inertial Flows and on Effective Hydraulic Parameters

Kuldeep Chaudhary

M. Bayani Cardenas

Wen Deng
Missouri University of Science and Technology, wendeng@mst.edu

Philip C. Bennett

Recommended Citation

K. Chaudhary et al., "Pore Geometry Effects on Intrapore Viscous to Inertial Flows and on Effective Hydraulic Parameters," *Water Resources Research*, vol. 49, no. 2, pp. 1149-1162, American Geophysical Union (AGU), Feb 2013.
The definitive version is available at https://doi.org/10.1002/wrcr.20099

WATER RESOURCES RESEARCH, VOL. 49, 1149–1162, doi:10.1002/wrcr.20099, 2013

Pore geometry effects on intrapore viscous to inertial flows and on effective hydraulic parameters

Kuldeep Chaudhary,[1] M. Bayani Cardenas,[1] Wen Deng,[1] and Philip C. Bennett[1]

Received 8 February 2012; revised 27 December 2012; accepted 9 January 2013; published 12 February 2013.

[1] In this article, the effects of different diverging-converging pore geometries were investigated, and the microscale fluid flow and effective hydraulic properties from these pores were compared with that of a pipe from viscous to inertial laminar flow regimes. The flow fields are obtained using computational fluid dynamics, and the comparative analysis is based on a new dimensionless hydraulic shape factor β, which is the "specific surface" scaled by the length of pores. Results from all diverging-converging pores show an inverse pattern in velocity and vorticity distributions relative to the pipe flow. The hydraulic conductivity K of all pores is dependent on and can be predicted from β with a power function with an exponent of 3/2. The differences in K are due to the differences in distribution of local friction drag on the pore walls. At Reynolds number (Re) $\sim$ 0 flows, viscous eddies are found to exist almost in all pores in different sizes, but not in the pipe. Eddies grow when $Re \rightarrow 1$ and leads to the failure of Darcy's law. During non-Darcy or Forchheimer flows, the apparent hydraulic conductivity K_a decreases due to the growth of eddies, which constricts the bulk flow region. At $Re > 1$, the rate of decrease in K_a increases, and at $Re >> 1$, it decreases to where the change in $K_a \approx 0$, and flows once again exhibits a Darcy-type relationship. The degree of nonlinearity during non-Darcy flow decreases for pores with increasing β. The nonlinear flow behavior becomes weaker as β increases to its maximum value in the pipe, which shows no nonlinearity in the flow; in essence, Darcy's law stays valid in the pipe at all laminar flow conditions. The diverging-converging geometry in pores plays a critical role in modifying the intrapore fluid flow, implying that this property should be incorporated in effective larger-scale models, e.g., pore-network models.

Citation: Chaudhary, K., M. B. Cardenas, W. Deng, and P. C. Bennett (2013), Pore geometry effects on intrapore viscous to inertial flows and on effective hydraulic parameters, *Water Resour. Res.*, *49*, doi:10.1002/wrcr.20099.

1. Introduction

[2] The geometry of pores controls intrapore fluid flow behavior that manifests as continuum-scale flow characteristics and hydraulic parameters. Therefore, a fundamental understanding of continuum-scale phenomenon is underpinned by a thorough understanding of pore-level fluid dynamics. Fluid dynamics at the pore scale has largely been studied using the classical capillary tube model, more recently by lattice Boltzmann methods [*Chukwudozie et al*., 2012; *Maier et al*., 1998, 1999; *Pan et al*., 2004; *Rothman*, 1988; *Yoon et al*., 2012], and pore-network models [*Balhoff and Wheeler*, 2009; *Blunt et al*., 2002; *Bryant and Blunt*, 1992; *Joekar-Niasar et al*., 2010].

[3] Capillary tube models assume a packing of spherical grains such that the flow pathways or fluid conduits can be represented by cylindrical tubes or capillaries. To consider or correct for the differences in grain shapes, *Kozeny* [1927], *Blake* [1922], and *Carman* [1938] introduced shape factors that represent capillary tubes with cross sections such as a circle, a square, or a triangle. Similarly, in pore-network models, the effect of grain shapes are represented by cross-sectional shapes such as a star, a square, and a triangle [*Blunt et al*., 2002; *Joekar-Niasar et al*., 2010; *Man and Jing*, 1999; *Valvatne et al*., 2005]. However, both capillary tube models and pore-network models still assume no variation, such as a realistic diverging-converging pore geometry in the direction of flow. Therefore, the complete effects of pore geometries in modifying the flow field are not well understood.

[4] Grains comprising geologic porous media can be very angular to round in shape, which results in flow channels having a diverse range of diverging-converging pore to pore-throat geometries. Few studies have investigated the fluid flow fields in idealized diverging-converging pores, but with simplistic pore geometries; for example, pore walls with sinusoidal curves [*Bolster et al*., 2009; *Bouquain et al*., 2012; *Dykaar and Kitanidis*, 1996; *Kitanidis and Dykaar*, 1997; *Malevich et al*., 2006; *Pozrikidis*, 1987; *Sisavath et al*., 2001], ellipses [*McClure et al*., 2010], a box shape [*Cao and Kitanidis*, 1998; *Ma and*

[1]Department of Geological Sciences, The University of Texas at Austin, Austin, Texas, USA.

Corresponding author: K. Chaudhary, Department of Geological Sciences, The University of Texas at Austin, 1 University Stn. C9000, Austin, TX 78712, USA. (kuldeep@austin.utexas.edu)

0043-1397/13/10.1002/wrcr.20099

Ruth, 1993, 1994; *Meleshko*, 1996; *Panfilov and Fourar*, 2006], tortuous pores [*Cardenas*, 2008; *Cardenas et al*., 2007; *Chaudhary et al*., 2011; *Fourar et al*., 2004], or periodic porous media [*Brenner and Adler*, 1982]. Moreover, most of the above-mentioned studies use Stokes flow or viscous flow, and only few inspect the flow fields in detail at increasing inertial flow regimes [*Chaudhary et al*., 2011; *Fourar et al*., 2004; *Leneweit and Auerbach*, 1999; *Ma and Ruth*, 1993; *Meleshko*, 1996; *Panfilov and Fourar*, 2006]. All the studies mentioned here notice eddies either during viscous flows or during inertial flow regimes, but none quantify the effect of growth in eddies and their feedback with different diverging-converging pore geometries in modification of the fluid flow field spanning from viscous to inertial flow regimes.

[5] Studying the effects of different diverging-converging pore geometries and eddies therein modifying fluid flow behavior bears important implications for addressing many critical issues including, for example, in natural settings, the flow and fate of nutrients and contaminants as mediated by microbes and biofilms [*Bennett et al*., 2000; *Guglielmini et al*., 2011], and in engineering applications, the pump and treat of aquifer contaminants, enhanced oil recovery operations, and geological storage of CO_2 [*Balhoff and Wheeler*, 2009]. In this paper, we specifically addressed the following questions: How does the geometry of diverging-converging pores control eddy behavior including its interaction with the bulk flow and effective hydraulic conductivity during viscous flows? How does the feedback between pore geometries and growth behavior of eddies determine Forchheimer flow characteristics?

[6] To address these related questions, we designed 10 diverging-converging pores and compared fluid flow characteristics and hydraulic properties from these pores with that of a pipe, which represents a capillary tube model and is the building-block for a pore-network model. We used a dimensionless hydraulic shape factor β to characterize and compare the different pore geometries. Microscale-steady laminar flow fields are obtained through computational fluid dynamics simulations, which represent flows from viscous to inertial regimes. Sensitivity analyses explore the role of different pore geometries (β) and related eddies on hydraulic conductivity, failure of Darcy's law, and characteristics of Forchheimer flows. Our analysis is focused on using fluid physics to examine the velocity and vorticity distributions inside pores and the force balance along pore boundaries.

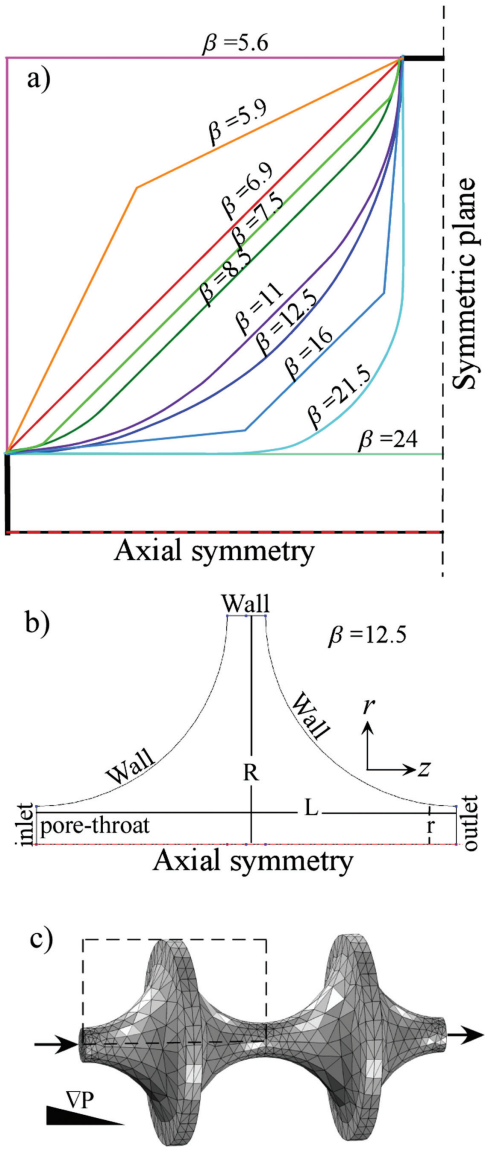

Figure 1. Diverging-converging pore geometry design: (a) half sections of 2-D pore design showing pore geometries formed due to arbitrary grain shapes (solid color lines) resulting in different hydraulic shape factors β; (b) a full 2-D section of a pore domain with $\beta = 12.5$; and (c) a full 3-D pore geometry of two periodic pores formed using the 2-D section from (b).

2. Methods

2.1. Pore Geometry Design

[7] We designed 10 different diverging-converging pore geometries likely formed due to arbitrarily round to angular grain shapes and a contrasting longitudinally uniform pore, which represents a capillary tube or a pipe domain (Figure 1a). The diverging-converging pore design is aimed to represent a grain packing of a cubic-type pattern with pore throats both in z and r directions (Figure 1b). These pore throats have an aspect ratio of 1:2 in r to z directions. The ratio of the radius at maximum divergence in pores to the radius of pore throats in z direction (R/r), and the length (L) in the z direction are the same for all pore domains. R is 1.2 $\times 10^{-3}$ m, r is 2×10^{-4} m, and L is 2.2×10^{-3} m.

[8] The pores are designed in two dimensions and have axial symmetry in the z direction along the bottom boundary of pore domains (Figure 1a). Therefore, we effectively studied the three-dimensional effects of pore geometries, which are diverging-converging in the z direction and have circular cross sections in the r direction, and compared them with a pipe domain.

2.2. Numerical Simulation Scheme

[9] Steady incompressible flow is governed by the Navier-Stokes and the continuity equations:

$$\nabla P = \mu\nabla^2\boldsymbol{u} - \rho(\boldsymbol{u}\cdot\nabla)\boldsymbol{u}, \quad (1)$$

$$\nabla\cdot\boldsymbol{u} = 0, \quad (2)$$

where ρ is fluid density, $\boldsymbol{u} = [u, v, w]$ is the velocity vector, μ is dynamic viscosity, and P is total pressure. Standard fluid properties for water are used: $\rho = 1000$ kg/m^3 and $\mu = 0.001$ Pa s. Numerical solutions are obtained via the finite-element method implemented with COMSOL Multiphysics [2008]. Lagrange-triangular elements were used to discretize the domain. About 10^5 elements were used based on a mesh-convergence analysis. The variations in the numerical solution at this level of mesh refinement are on the order of $<0.01\%$. The governing equations were cast and solved in cylindrical coordinates (r, z).

[10] The bottom boundaries along the length of pores in the z direction are an axial symmetry (Figure 1). The grain surfaces and the pore throats in the r direction follow a no-slip or a wall boundary condition. Pore throats in the z direction are inlet and outlet boundaries, which are prescribed with a pressure gradient. The inlet and outlet boundaries are also the periodic boundaries that aid in obtaining a fully developed flow and a flow field representative from a single pore of an infinite sequence of pores (Figure 1c). The pressure gradients are systematically increased from 10^{-3} (Pa) to 200 (Pa) across the pores to obtain steady-state laminar flow fields of *Re* from approximately 0 to 250.

2.3. Dimensionless Parameters

2.3.1. Hydraulic Shape Factor β

[11] We quantified the pore geometry by introducing a dimensionless hydraulic shape factor β:

$$\beta = \frac{S_A \times L}{V}, \quad (3)$$

where S_A is the surface area of axis symmetric pores, V is the pore volume, and L is the length of domain in z direction. We used β as a metric to quantify the sensitivity of hydraulic properties to pore geometry. β is similar to the specific surface and hydraulic radius concepts [*Bear*, 1972; *Saeger et al*., 1991, 1995], which was originally used by *Kozeny* [1927] for predicting permeability of nondiverging-converging capillary tubes.

[12] The design of pore geometries as described in section 2.1 contribute to a spectrum of β factor values spanning from 5.6 to 24. For example, β 12.5 corresponds to a pore domain formed by a cubic-type pattern of circular grain shapes, and β 24 represents a pipe domain (Figure 1).

[13] In section 3, at times we chose to show results from fewer pore domains, which nonetheless are representative of low, intermediate, and high β values. When deemed more appropriate, we used results from all the pore domains for a detailed analysis. We followed this approach to improve clarity in presentation of our results, yet capture the controls of β. However, all the 11 pore domains we modeled were extensively analyzed.

2.3.2. Darcy's Law and the Hydraulic Gradient *i*

[14] *Darcy*'s [1856] empirical relationship was later theoretically derived and came to be known as Darcy's law, which in one-dimensional form is:

$$\frac{Q}{A} = q = K\left(\frac{\partial h}{\partial z}\right)^n; n = 1, \quad (4)$$

where Q is volumetric discharge (m^3/s), q (m/s) is Darcy flux, A is the cross-sectional area, h is hydraulic head equivalent to $P/\rho g$, where g is acceleration due to gravity, and K is hydraulic conductivity, which is related to intrinsic permeability (k) as:

$$K = \frac{k\ \rho\ g}{\mu}. \quad (5)$$

[15] The hydraulic gradient i is:

$$i = \frac{\partial h}{\partial z}. \quad (6)$$

[16] We used $q \propto i^n$ relationship (4) to obtain K of different pore domains. In equation (4), $n = 1$ corresponds to a flow regime where Darcy's law is valid, and when $n < 1$, the flow is known to be non-Darcy or Forchheimer flow. The slope of $q(i^n)$ when $n = 1$ is K, and when $n < 1$ is the apparent hydraulic conductivity K_a.

2.3.3. Reynolds Number

[17] To quantify the relative importance of inertial forces to viscous forces and to compare flow fields between different pore geometries, we used the Reynolds number *Re*, which is calculated as:

$$Re = \frac{\rho\ \overline{U}\mathrm{d}_0}{\mu}, \quad (7)$$

where $\overline{U}$ is the average velocity at the inlet and d_0 is the inlet diameter. Note that $\overline{U}$ and q in (4) are the same for pore domains in this study.

3. Results and Discussion

3.1. Viscous Eddies

[18] At steady laminar flow conditions of $Re \sim 0$ and i on the order of 10^{-5}, we observed eddies in all diverging-converging pores, except the pore with $\beta = 5.9$ (corner angle $> 170°$). At $Re \sim 0$ flow conditions, Figure 2a shows eddies in three pores with β of 6.9, 8.5, and 12.5, where these eddies occupy about 33%, 11%, and 2.5% of total pore volumes, respectively. These eddies, even though they are present at $Re \sim 0$ flow conditions, do not influence the Darcy relationship. Such eddies that occur in flows dominated by the viscous forces are often called viscous eddies, Stokes eddies, and Moffatt eddies [*Moffatt*, 1964]. Viscous eddies inside pores, cavities, and boundary wedges/corners are well studied in numerical and laboratory experiments [*Cardenas*, 2008; *Chaudhary et al*., 2011; *Cheng and Hung*, 2006; *Collins and Dennis*, 1976; *Hasimoto and Sano*, 1980; *Meleshko*, 1996; *Obrien*, 1972; *Shen and Floryan*, 1985; *Taneda*, 1979].

[19] The volume of viscous eddies or their sizes are significantly different between different pore domains. We found no relationship between the hydraulic shape factor β and the size or the occurrence of these eddies. The size of these eddies are dependent on how close grain boundaries

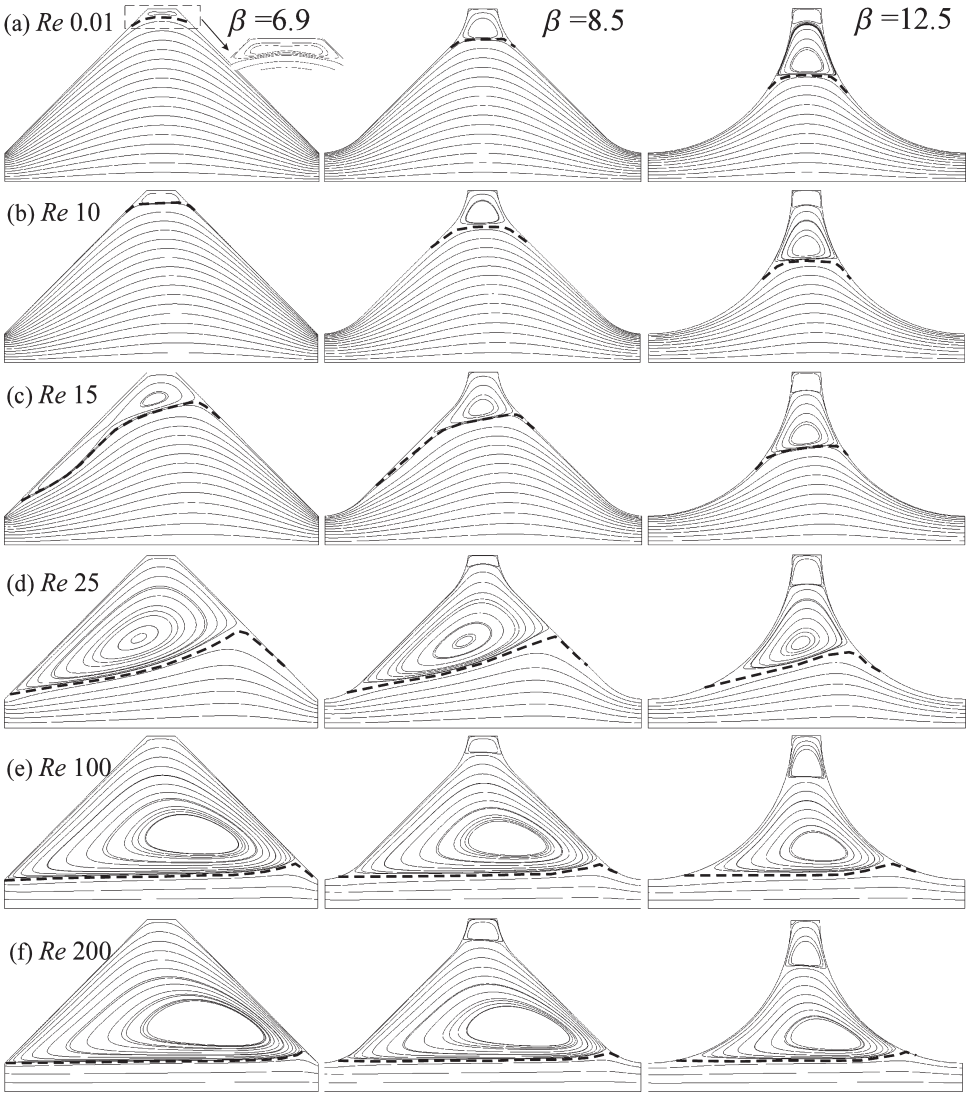

Figure 2. Flow fields from three different pore geometries showing eddies in (a) Darcy flow regime and their growth (a–f) as fluid flow increases from *Re* 0.008 to *Re* 200 to occupy a large part of the advective pore volume (n_e). Flow is from left to right. Black lines are the streamlines, and bold black dashed lines separate the eddies and the n_e.

are to each other, i.e., the wedging of grain boundaries around dead-end pores, which results in stagnation zones. The bulk flow bypasses stagnation zones as a measure to minimize the dissipation of momentum and contribute to fluid rotation in stagnation zones.

3.2. Velocity Distribution

[20] To study the variations in fluid flow behavior induced as a result of different pore geometries, we examined the distribution patterns of the magnitude of velocity ($|U|$) and the modulus of vorticity ($|\omega|$) from four different pore domains, which represent the hydraulic shape factor β values of 6.9, 8.5,12.5, and 24 (Figure 3). The differences in the flow behavior between different pores are later compared with flows spanning from viscous to inertial flow regimes. As the flow regimes become inertia dominated, the viscous eddies begin to grow, and therefore, we were able to analyze the modification in the flow associated with eddy growth. $|U|$ and $|\omega|$ are normalized by the maximum value among all four pore domains in context here. This allows us to compare differences both in the distribution patterns and the magnitude differences in $|U|$ and $|\omega|$ across different pores.

[21] The steady-state laminar flows from $i = 5 \times 10^{-5}$ to 4.37 or *Re* ~0 to ~200 show that the diverging-converging pore geometry leads to an inverse distribution pattern in $|U|$ relative to the pipe. Pipe flow is dominated by high velocities, whereas the diverging-converging pores (with β of 6.9, 8.5, and 12.5) are dominated by low velocities (Figure 3).

[22] The value of the highest velocity in a pore increases with a decrease in β. The value of the lowest velocity in a pore decreases with an increase in β. These differences in the highest and the lowest velocities between pores converge toward similar values as viscous flows progressively become inertial (Figures 3a–3e). For example, during flows of $i = 5 \times 10^{-5}$ or *Re* ~0 (Figure 3a), the pore with $\beta = 6.9$

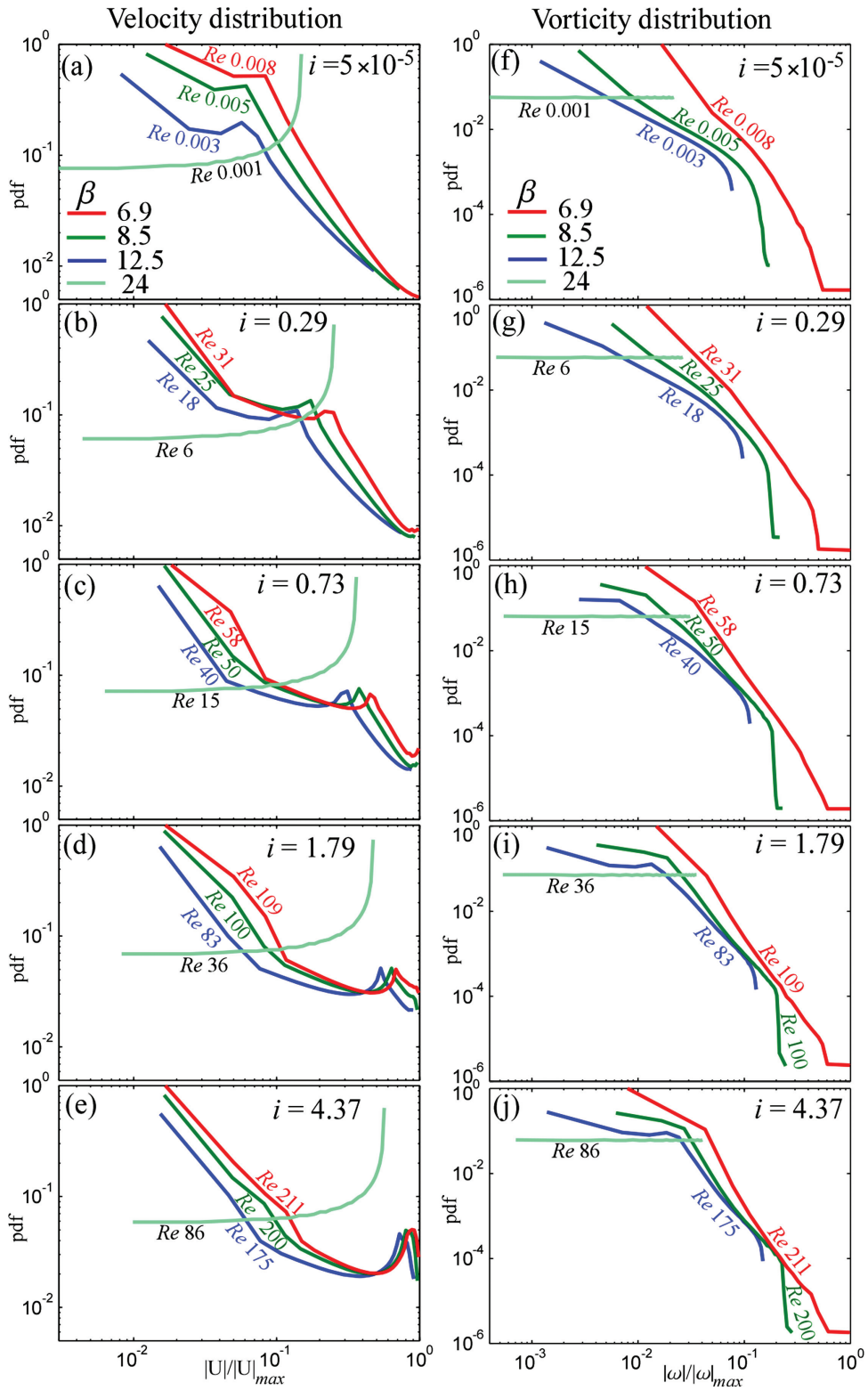

Figure 3. Probability distribution functions (pdf) showing the distribution patterns of the magnitude of velocity ($|U|$; a–e) and the absolute value of vorticity ($|\omega|$; f–j) from pores and the pipe during viscous (first row; a and f) to inertial flow regimes (succeeding rows; b–e and g–j).

has the maximum velocity, which is six times greater than the pipe ($\beta = 24$), and the pipe has the minimum velocity, which is 10 times smaller than the pore with $\beta = 6.9$. At flows of $i = 4.37$ or $Re \sim 200$, differences both in the maximum and the minimum velocities between these two domains are reduced to only twice as much (Figure 3e).

[23] The diverging-converging pore geometry leads to a significant increase in the spread of $|U|$ distribution relative

to the pipe. The breadth in the distribution of $|U|$ shows an increasing trend with a decrease in β. The spread in $|U|$ distributions is the largest during viscous flows and becomes progressively narrower as the flows become inertial.

[24] Figures 3a–3e show the peaks in the velocity distribution that are associated with the nature of boundary between the eddies and the advective flow channel, i.e., the area of n_e in Figure 2. The velocity distribution to the right of these peaks (higher $|U|$) is from the advective flow channel, whereas to the left of the peaks is the velocity distribution from the eddies. As the flow becomes increasingly inertial, these peaks shift toward a higher $|U|$ and a lower predominance, which is due to the shifting of boundary between eddies and the advective flow channel toward the bulk flow as a result of growth in eddies. The $|U|$ increases with increasing *Re* flows in the bulk flow (n_e), and due to the growth in eddies, the area occupied by advective flow channel decreases, which results in a lower predominance. The part of $|U|$ distribution to the left of the peaks shows the evolution of $|U|$ distribution inside eddies as flows continue to gain inertia (Figures 3a–3e).

[25] The large differences in the distribution pattern and the spread of $|U|$ values between pores during viscous flow are due to the flow field modifications associated with pore geometry, which results in different radius of advective flow channel (i.e., different viscous dissipation) and different size of eddies (i.e., low velocities). However, during inertial flows, these differences between pores are minimized, and pore geometry seems to play a less significant role because eddies in pores all grow to their maximum size and shrink advective flow channel to a similar size (Figures 2a–2f), which results in a focused flow characteristic similar to each other (Figure 3e). We continue this discussion about the role of pore geometry in flow modification in sections 3.5 and 3.6.

3.3. Vorticity Distribution

[26] Vorticity (ω), which is $\nabla \times \boldsymbol{u}$, measures the rate of rotation of a fluid element in the flow field. Vorticity is associated with the no-slip boundary at the pore walls, and it diffuses and advects to the interior of the flow field [*Lugt*, 1996]. The presence of eddies produces locally high vorticity. In viscid flow with no-slip boundaries, $\omega \neq 0$; however, this does not imply the existence of eddies. On the other hand, there are no eddies without vorticity. The presence and the size of eddies at $Re \sim 0$ flows depend mainly on the wedging of grain boundaries around dead-end pores. In many ways, these are similar to "Moffatt eddies" around corners [*Moffatt*, 1964].

[27] Figure 2 illustrates the sizes and the location of eddies in different pores from viscous to inertial flow regimes, and here we examined the distribution patterns in the modulus of vorticity ($|\omega|$) from the pores with β of 6.9, 8.5, 12.5, and 24. The $|\omega|$ values are normalized by the maximum value among all the pores.

[28] During the steady viscous flows, i.e., $i = 5 \times 10^{-5}$, or the inertial flows (Figures 3b–3e), the diverging-converging pores show a large variation in the distribution of $|\omega|$ in comparison with the pipe flow (Figure 3a). The pipe flow, as already theoretically established, shows a uniform and constant vorticity distribution at all flow conditions. Between the three diverging-converging pores, the differences in the range of $|\omega|$ are pronounced during the viscous flows; however, these become narrower during increasing inertial flows.

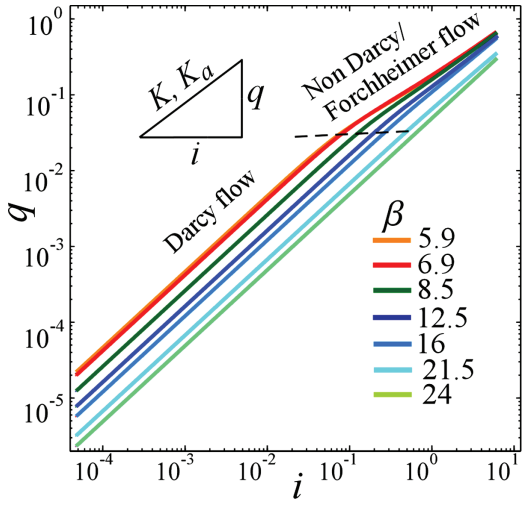

Figure 4. Fluid flux, q (m/s), and hydraulic gradient, i, relationship showing differences in hydraulic conductivity, K (m/s), between the pores and a pipe. Note, the q of pores begin to converge at $i > 1$.

[29] The magnitude of vorticity exhibits an increasing trend with a decreasing β. The pore with $\beta = 6.9$ shows the widest range in vorticity distribution. It has both the highest vorticities, yet also shows a higher predominance of low vorticities when compared with pores with β of 8.5 and 12.5 (Figure 3). Similarly, the distribution of vorticity (Figure 3) also increases with decreasing β. However, the $|\omega|$ distribution for a given pore does not show any significant change as the flows transition from viscous to increasingly inertial flow regimes (Figures 3b–3e).

[30] The uniform vorticity distribution within the pipe is due to the linear dissipation of friction drag, whereas the large variations in vorticity and its broad distribution in different diverging-converging pores indicate that the stress field gets significantly modified by the diverging-converging pore geometry. These differences in the pattern of stress distribution between pores begin to diminish as the flows progressively become inertial, yet the stress fields remain significantly different, for example, at $i = 4.37$ (Figure 3e).

3.4. Hydraulic Conductivity *K* and the Hydraulic Shape Factor β

[31] To quantify the effects of pore geometry on K, we used a $q \propto i^n$ relationship following Darcy's law (4). A sequential increase in pressure (P) from 10^{-3} Pa to 200 Pa is imposed at the inlet boundaries (pore throats), and Q is obtained for a total of 11 pores. Following equation (4), the K or K_a is calculated (Figure 4). In $q \propto i^n$ relationships, $n = 1$ corresponds to Darcy flow, and when $n < 1$, flow is known to be non-Darcy or Forchheimer flow (Figure 4). The slope of $q(i^n)$, when $n = 1$ is the K, and when $n < 1$ is the K_a. In this section, we only discuss flow modification in pores when $n = 1$, whereas variations in the flow field when $n < 1$ are discussed in sections 3.8 and 3.9.

[32] From the calculated K of a range of pores with their hydraulic shape factor spanning from $\beta = 5.6$ (a pore with a

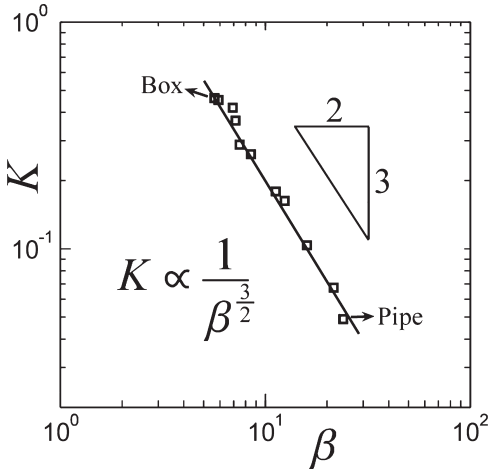

Figure 5. The hydraulic conductivity, K (m/s), is inversely related to hydraulic shape factor β by a power law with an exponent of 3/2 ($R^2 = 0.99$).

box-shaped pore geometry) to $\beta = 24$ (the pipe; Figure 1a), we found that there is an inverse power-law relationship between K and β (Figure 5), which has an exponent of 3/2. This relationship follows the form:

$$K \propto \frac{1}{\beta^{\frac{3}{2}}}, \tag{8}$$

[33] Equation (8) is similar in form to *Kozeny*'s [1927] equation, which is given as:

$$K \propto \frac{\phi^3}{M^2}, \tag{9}$$

where ϕ is porosity and M is the specific surface or the hydraulic radius equivalent to S_A/V. $\phi = 1$ in all our pores, and their lengths (L) are also the same; therefore, β and M in equations (8) and (9) are analogous. Equation (9) describes variations in the K as a function of variations in the radius of pipes, whereas equation (8) describes variations in the K as a result of different diverging-converging pore geometries having some characteristic radius proportional to β. Equation (8) represents the exact effect of diverging-converging pore geometries on K; however, the usage of an average effective radius for the diverging-converging pores and using Kozeny's equation will lead to an over prediction in variations in K. Nowadays, β can be readily quantified from observations by using techniques such as X-ray tomography. Thus, equation (8) can be used to determine the theoretical and exact K of pores, which in turn can be used in the pore-network models.

3.5. Drag Forces and Hydraulic Conductivity *K*

[34] In the previous section, we observed that the K decreases with an increase β. Here we present a more detailed examination of how the pore geometry (as represented by β) controls the continuum flow behavior, which is manifested in K.

[35] Hydraulic conductivity is a manifestation of the total resistive forces inside a pore. The total resistive force due to the pore boundary is the total drag (F_D), whose components are the friction drag (F_τ) and the form drag (F_N), i.e., $F_D = F_N + F_\tau$. We examined all three drag forces individually to evaluate which of these forces actually determines the effective hydraulic parameter (K).

[36] The z component of local form drag and local friction drag in cylindrical coordinates is:

$$f_{N,z} = -[(P \quad \mathbf{I}) \cdot \boldsymbol{n}_z], \tag{10}$$

$$f_{\tau,z} = \quad \eta\left[\left(\frac{\partial u}{\partial z} + \frac{\partial v}{\partial r}\right) \cdot \boldsymbol{n}_r + 2\left(\frac{\partial v}{\partial z}\right) \cdot \boldsymbol{n}_z\right]. \tag{11}$$

[37] where $\boldsymbol{I}$ is the identity matrix, η is the dynamic viscosity, u and v are velocities in r direction and z direction, respectively, and $\boldsymbol{n}_r$ and $\boldsymbol{n}_z$ are unit vectors in r and z directions, respectively. Note that in our convention, friction drag on the pore boundary is negative in the flow direction ($+z$) and vice versa.

[38] For axis symmetric tubes, the average form drag F_N is calculated by integrating the z component of the local form drag over the surface of the pore domain:

$$F_N = \left|\frac{\int f_{N,z} \cdot \boldsymbol{n} \; \mathrm{d}A}{\int \mathrm{d}A}\right|, \tag{12}$$

where $\boldsymbol{n}$ is a unit vector normal to pore boundaries. Similarly, the average friction drag F_τ is calculated by integrating the z component of the local friction drag over the surface of the pore body as:

$$F_\tau = \quad \left|\frac{\int \boldsymbol{f}_{\tau,z} \cdot \boldsymbol{t} \; \mathrm{d}A}{\int \mathrm{d}A}\right|, \tag{13}$$

where $\boldsymbol{t}$ is the unit vector tangent to pore boundaries. (Since the integration of the r components of form drag and friction drag over the surface of an axis symmetric tube yields zero, they are not included here.) Note that we calculated the magnitude of F_τ, i.e., its absolute value; however, the average F_τ is <0 in all pores, but presented as positive values.

[39] We examined the role of F_N, F_τ, or their sum F_D in controlling the K from three different diverging-converging pore geometries with β values of 6.9, 8.5, and 12.5. In this section, we discuss the role of these force on K, i.e., the Darcy flow regime, and in the subsequent section 3.9, we focus on the non-Darcy or Forchheimer flow regime.

[40] We found that the total drag F_D does not explain the variations in the K of different pores; F_D is the same for different pores and shows a similar rate of linear increase as flows increase from Re 0 to $Re \gg 1$ (Figure 6a). In fact, F_D is expected to be the same due to the force balance and the design of pores. As the same hydraulic gradient i is imposed on all pores and they have the same cross-sectional area (at the pore throat), their F_D is the same following the force balance equation: $F_D = i \cdot A$. However, as K is different for different pores, whereas F_D is the same, F_D

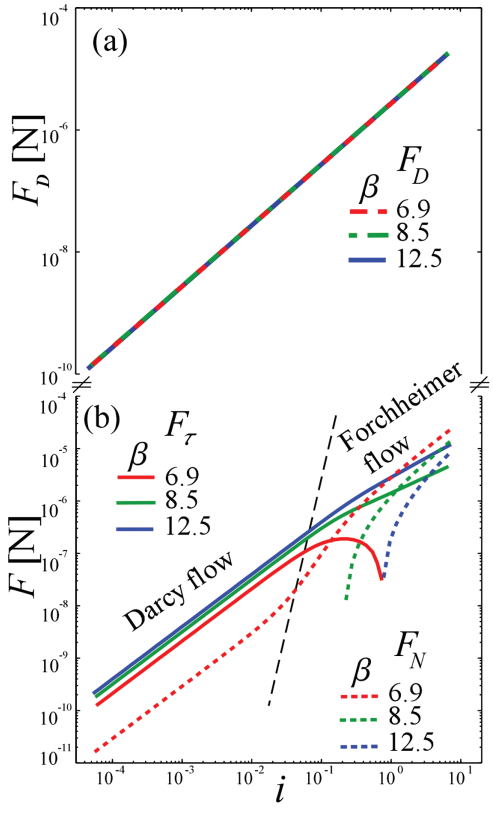

Figure 6. Average net drag forces: (a) total drag F_D [N] and (b) friction drag F_τ [N] and form drag F_N [N], from pore boundaries during Darcy to Forchheimer flow regimes.

has no role in determining the difference in K or K_a. F_D and its relation to K_a are further discussed in section 3.9.

[41] We found that the friction drag F_τ is the resistive force that can explain for the differences in K of pores. F_τ shows an increase with β, whereas the K decreases with an increase in β. The pore with a higher F_τ has a lower K and vice versa. For example, the pore with $\beta = 12.5$ has F_τ 1.5 times greater than the pore with $\beta = 6.9$ and 1.06 times greater than the pore with $\beta = 8.5$ (Figure 6). In comparison with F_τ, F_N is about a magnitude smaller in the pore with $\beta = 6.9$ and ~0 in pores with $\beta = 8.5$ and 12.5 (Figure 6b). During the Darcy flow regime, the F_N is either insignificant or nil, and F_τ emerges as the dominant resistive force that contributes to the differences in K.

3.6. The Distribution of Friction Drag

[42] In the previous section, we found that F_τ controls the differences in K. However, why does friction drag differ for different pores? How does pore geometry influence F_τ? To examine these questions, we present further examination of the distribution of local friction drag $f_{\tau,z}$ along the pore walls. Three different diverging-converging pore geometries with β values of 6.9, 8.5, and 12.5 and the pipe domain ($\beta = 24$) are analyzed (Figure 7). Here we examined $f_{\tau,z}$ distribution during the Darcy flow regime, and the evolution in $f_{\tau,z}$ distribution as the flows become non-Darcy and when the eddies grow are discussed in the section 3.9.

[43] The $f_{\tau,z}$ is large near pore throats and decreases with increasing pore radii and distance away from the bulk flow direction (Figure 7). The negative friction drag ($-f_{\tau,z}$) is due to the flow from left to right (Figure 7) or the clockwise rotation of eddies, and the positive friction drag ($+f_{\tau,z}$) is associated with counterclockwise rotation of eddies. The part of boundaries with warm colors indicate counterclockwise eddies, and the part with cool colors indicate clockwise eddies. In Figure 7, the individual color-filled circles (dots) in dead-end corner of pores are due to corner eddies similar in form to Moffat's eddies. These corner eddies were not visible in Figure 2a, and thus, Figure 7 provides another way to perceive the existence of such eddies.

[44] $f_{\tau,z}$ is proportional to the velocity gradient in r direction, which is higher around the pore throats. During Darcy flows, the amount of $f_{\tau,z}$ near pore throats accounts for the most of net friction drag (F_τ) in a pore (Figure 7a). The amount of $f_{\tau,z}$ from the pore body is relatively small and insignificantly influence F_τ. The pore with $\beta = 12.5$ has a larger section of pore boundary near the pore throats relative to the pores with β of 8.5 and 6.9 (Figure 7a). The larger pore boundary near the pore throats accounts for a larger $f_{\tau,z}$ and consequently a larger F_τ. The portion of pore boundary near the pore throats decreases with a decreasing β, and therefore, the pores with increasing β in order of 8.5, 6.9, 12.5, and 24 offer an increasing larger F_τ in the same order (Figure 6b) and consequently result in a decreasing trend in K of pores with increasing β (Figure 5).

[45] We found that the local friction drag controls K within the Darcy flow regime and is largely influenced by the pore geometry near pore throats. Therefore, the observed differences in the K of pores are due to the variations in distribution of $f_{\tau,z}$ on the pore boundary, specifically near pore throats.

3.7. Pore Geometry and the Failure of Darcy's Law

[46] We have shown that Darcy's law begins to fail because of the growth in pre-existing viscous eddies inside pores with increasing inertia [*Chaudhary et al.*, 2011]. Here we examined the effect of pore geometry β factor on the onset of the eddy growth and effectively the failure of Darcy's law, i.e., when $n \neq 1$ in equation (4). We used seven different diverging-converging pores and calculated the friction drag (F_τ; equation (13)) from pore boundaries (Figure 1, "Wall") during flows spanning viscous to inertial flow conditions. During $Re < 1$ flow conditions, F_τ linearly increases with an increase in i or the corresponding increase in velocity flux. With an increase in i around $Re < 1$ flow conditions, viscous eddies are stationary and show no sign of growth. As the flow conditions increase to $Re > 1$, viscous eddies begin to grow, and an increasingly larger area of the pore boundary is subjected to counter flow, which contributes to oppositely directed friction drag. Therefore, the rate of increase in F_τ with i (i.e., F_τ'; equation (14)) is constant during $Re < 1$ flow conditions, and at increasing flow conditions ($Re > 1$), i.e., when inertia begins to become dominant or eddies begin to grow, the rate of increase in F_τ with i becomes nonlinear or shows a decrease due to the oppositely directed friction drag contributions from the growth in eddies. Henceforth, we use the nonlinearity in F_τ' as a proxy for the growth in eddies. The rate of change in F_τ with increasing i is:

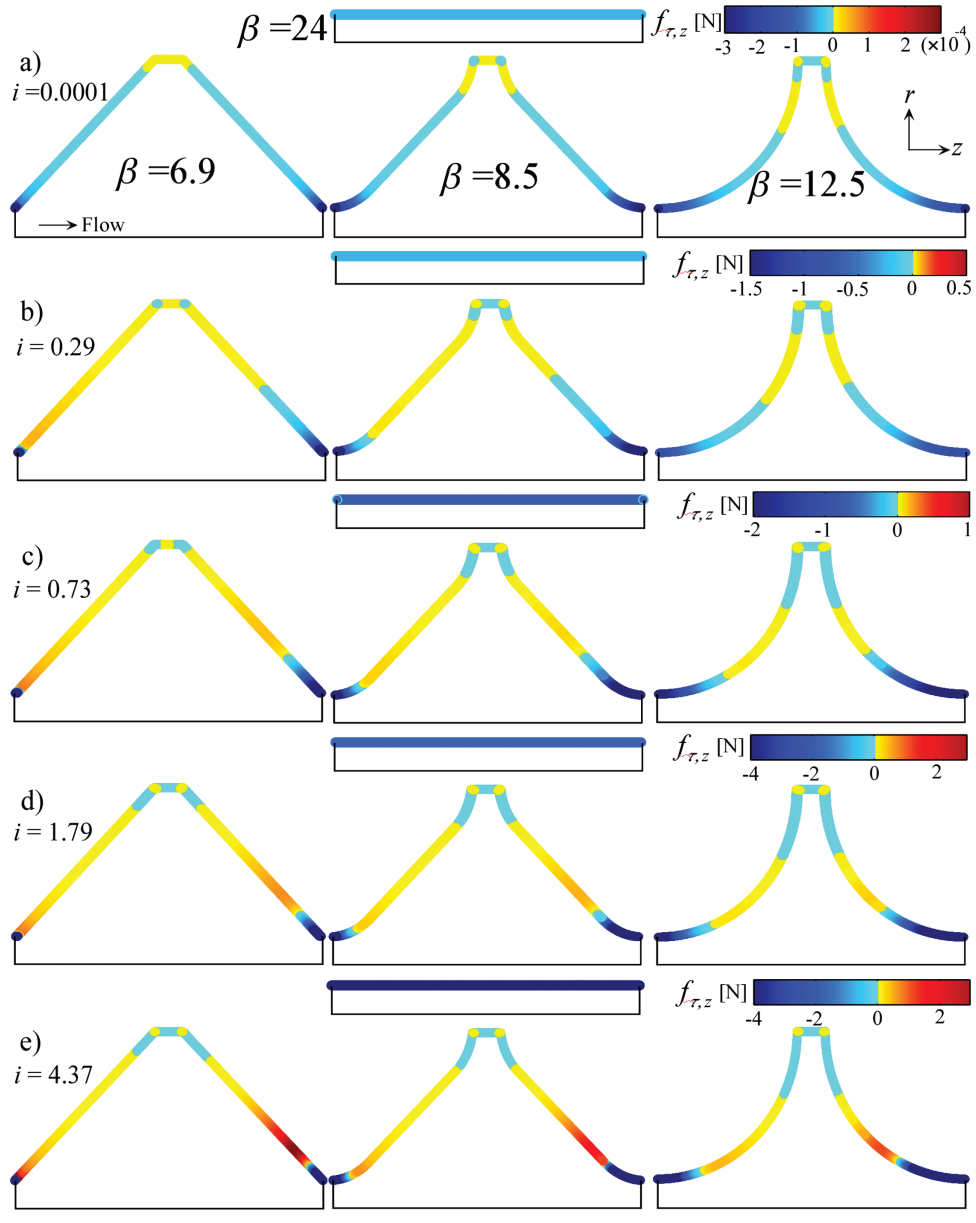

Figure 7. Local friction drag $f_{\tau,z}$ [N] distribution on the boundaries of the pores and a pipe from Darcy to non-Darcy flow regimes. Negative $f_{\tau,z}$ is due to flow from left to right or the clockwise flow of eddies, and positive $f_{\tau,z}$ is due to the counterclockwise flow of eddies.

$$F_\tau' = \frac{\partial F_\tau}{\partial i}. \tag{14}$$

[47] Corresponding to the functional form $q(i)$, we define an apparent hydraulic conductivity (K_a) following (4). *Chaudhary et al*. [2011] have shown that the nonlinearity in Darcy's K is due to the growth of eddies in pores. Furthermore, the onset of eddy growth corresponds to the onset of nonlinearity in F_τ' [*Chaudhary et al*., 2011]. Likewise, we used the nonlinearity in F_τ' as an indicator for eddy growth and the failure of Darcy's law.

[48] Figure 8a shows K or K_a variations with increasing i for seven different diverging-converging pores. Similar to *Chaudhary et al*. [2011], the critical flow condition (i or Re) at which K departs from the linearity in all pores is congruent to the critical i or Re, which marks the nonlinearity in F_τ' (Figure 8). The critical i or Re that marks the failure of Darcy's law shows an increasing trend for pores with an increasing β. The nonlinearity in K or K_a occurs at the lowest hydraulic gradient ($i = 0.005$ or $Re = 0.5$) in the pore with the smallest β of 5.9. The nonlinearity in K or K_a occurs at increasing i conditions for pores having increasingly higher β. For example, in pores with $\beta = 12.5$ and 16, the nonlinearity in K occurs at $i = 0.016$ or $Re = 1$ and $i = 0.025$ or $Re = 1.6$, respectively. However, no unique relationship between the pore β and the critical i, at which K becomes nonlinear, can be established.

[49] Nonetheless, the trend we noticed between critical i or Re that marks the failure of Darcy's law and β (Figure 8) indicate some control of β in the advent of growth in

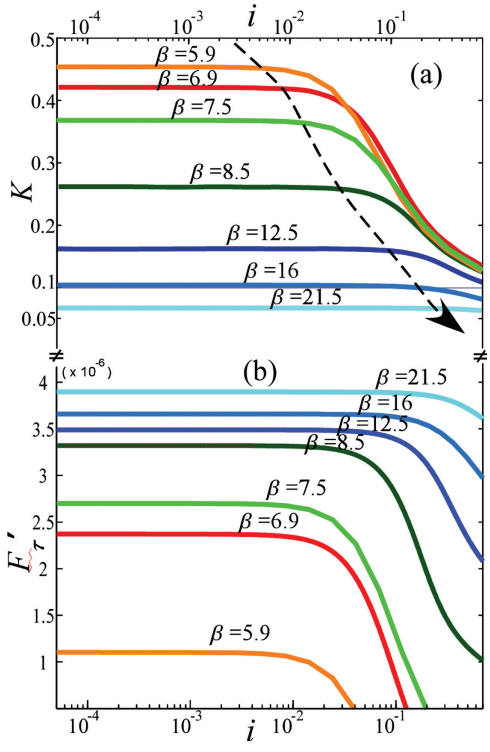

Figure 8. The failure of Darcy's law at increasing hydraulic gradient i is indicated by the onset of nonlinearity (marked by dashed lines) in (a) hydraulic conductivity K (m/s) and (b) rate of change in friction drag F'_τ [N] with increasing i, which are both due to the growth in eddies.

eddies. Eddies grow first or at a lower i or Re in the pore with a smaller β because vorticities are higher in pores with smaller β. For example, the pore with $\beta = 12.5$ has relatively lower vorticities than the pore with $\beta = 6.9$, which has relatively higher vorticities (Figure 3f). Thus, it takes higher Re flows (more inertia) in the $\beta = 12.5$ pore to increase vorticity to a similar magnitude as the $\beta = 6.9$ pore at which eddies begins to grow. In contrast to the above results, the pipe exhibits no nonlinearity in K or failure of Darcy's law (Table 1) as eddies are absent in the pipe flow.

3.8. Pore Geometry and Characteristics of Forchheimer Flow

[50] At $Re >> 1$ flow conditions, the nonlinearity in $q(i)$ relationship is described by a modified Darcy's law or the Forchheimer relationship, which in quadratic form is given as:

$$-i = a\,q + b\,q^2, \tag{15}$$

where a and b are coefficients of the polynomial fit. From equations (4) and (15), $1/K_a = a + b\,q$. Although much theoretical development and their validation by numerical models have been done to derive the Forchheimer relationship [*Chen et al.*, 2001; *Fourar et al.*, 2004; *Hassanizadeh and Gray*, 1987; *Ma and Ruth*, 1993; *Meleshko*, 1996; *Panfilov and Fourar*, 2006; *Skjetne and Auriault*, 1999], many forms of Forchheimer flow laws such as a power function, a quadratic equation, and a cubic equation have been proposed [*Balhoff and Wheeler*, 2009; *Chen et al.*, 2001; *Cheng et al.*, 2008; *Panfilov and Fourar*, 2006; *Skjetne and Auriault*, 1999]. Although the nonlinearity or the power relationship in the functional form of $q(i)$ have been derived from first principles, the existence of different forms of Forchheimer relationships remains enigmatic.

[51] Here we studied the role of β and eddy behavior in different pores on the Forchheimer relationships during $Re >> 1$ flow conditions. We present results from five different diverging-converging pore geometries with β values of 5.6, 6.9, 8.5, 12.5, and 16.

[52] We have previously shown that the physical mechanism that governs the Forchheimer flow characteristics is associated with the growth behavior of eddies, which in turn is of course expected to be sensitive to pore geometry. During Forchheimer flows, K_a decreases systematically due to the decrease in "advective flow channel," which is a result of the growth in eddies at increasing Re flows [*Chaudhary et al.*, 2011]. During increasing Re flows, this characteristic decrease in K_a is at first an increase in the rate of decrease in K_a (i.e., $-K'_a$) and later a decrease in the rate of decrease in K_a ($-K'_a$; Figure 9). At $Re >> 1$, this rate of decrease in K_a, i.e., $-K'_a \approx 0$, and flows once again exhibit a Darcy-type relationship. We define K'_a as the second derivative of q with respect to i following equation (14).

[53] At the onset of Forchheimer flow, different pores have different K_a, which tend to converge at flows of $Re >> 1$ (Figure 4). To describe flows spanning $Re \sim 0$ to $Re >> 1$, we found equations that fit the data with $i \propto q^m$ relationship, where $m = 1/n$ (Table 1). For all pores, except the pipe flow, $m = 2$ with $R^2 = 0.999$ and $m = 3$ with $R^2 = 1$. In contrast, $m = 1$ in the pipe flow, i.e., Darcy's law stays valid at $Re >> 1$.

[54] We further examined the effects of pore geometry on the Forchheimer flow characteristics by examining variations in the growth rate of eddies and variations in the rate of decrease in K_a (i.e., $-K'_a$) during increasing Re flows. The eddy growth rate is represented by the rate of change in the rate of decrease in friction drag, i.e., $-F''_\tau$, and compared with the rate of decrease in apparent hydraulic conductivity, i.e., $-K'_a$ (Figure 9). $-F''_\tau$ is the second order derivative with respect to i following equation (14).

[55] In all pores, $-F''_\tau$ shows a direct relationship to $-K'_a$, but with some lag (Figure 9). In the beginning of Forchheimer flow conditions, both $-F''_\tau$ and $-K'_a$ are

Table 1. Hydraulic Conductivity, K (m/s), and $q(i)$ Relationship From Darcy to Forchheimer

β	K (m/s)	Darcy to Forchheimer Flows
5.6	0.4626	$i = 12.147q^2 + 4.734q - 0.0328$
5.9	0.4518	$i = 6.9212q^2 + 5.273q - 0.038$
6.9	0.4209	$i = 4.4918q^2 + 5.7209q - 0.0502$
7.15	0.3678	$i = 6.374q^2 + 5.3833q - 0.0339$
7.5	0.2881	$i = 5.4921q^2 + 6.04q - 0.0303$
8.5	0.2615	$i = 3.8825q^2 + 6.6084q - 0.036$
11	0.1794	$i = 4.92q^2 + 7.49q - 0.0211$
12.5	0.1627	$i = 3.516q^2 + 8.34q - 0.0254$
16	0.1037	$i = 2.27q^2 + 9.66q - 0.014$
21.5	0.0674	$i = 5.07q^2 + 15.5q - 0.0047$
24	0.049	$i = 20.408q^1$

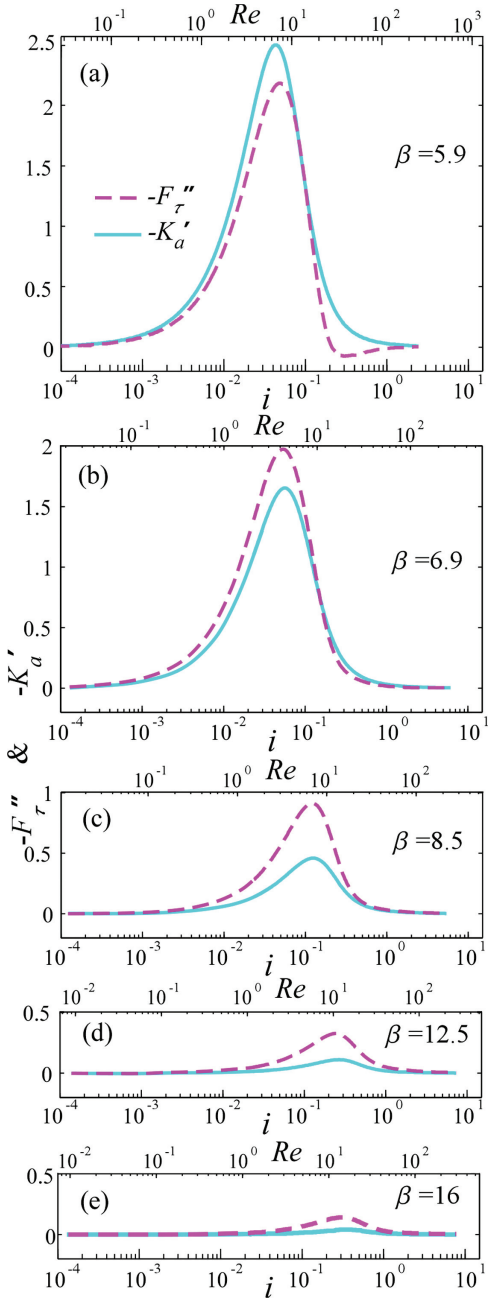

Figure 9. Forchheimer flow characteristics showing the rate of decrease in apparent hydraulic conductivity $-K'_a$ (m/s) and the rate of decrease in F'_τ, i.e., $-F''_\tau$ [N] with increasing hydraulic gradient i.

small, which then increase to a maximum (peak) at further increase in Re, and later both of them decrease to approximately 0 at even higher Re flows (Figure 9). The increase in $-F''_\tau$ and $-K'_a$ indicates how fast eddies grow or how fast K_a decreases with a flow increase from $Re \sim 1$ to $Re > 1$. Similarly, the decrease in $-F''_\tau$ and $-K'_a$ from their peak values to approximately 0 indicates how fast the growth in eddies ceases or how fast the decreases in K_a asymptote to a near constant value with a continued flow increase from $Re > 1$ to $Re >> 1$. The magnitude of peaks indicates how much decrease in K_a occurs in a given pore or how large eddies can grow in that pore. The height of these peaks or the net decrease in K_a shows an inverse relationship with β. The peaks in $-F''_\tau$ and $-K'_a$ are the maximum in the $\beta = 5.9$ pore and decreases with increase in β. For example, in the $\beta = 16$ pore, the peaks in $-F''_\tau$ and $-K'_a$ are approximately 10 times smaller than the pore with $\beta = 5.9$ pore, and negligible in the $\beta = 21.5$ pore (not shown in Figure 9 as they were unnoticeable). The magnitude of the peaks in $-F''_\tau$ or $-K'_a$ is an indicator for the degree of nonlinearity in the $q(i)$ relationship. The nonlinearity in $q(i)$ relationship becomes smaller and smaller as the pore β approaches that of the pipe. In addition, there is no nonlinearity in $q(i)$ relationship in the pipe flow (see Table 1, $\beta = 24$).

[56] The maximum of $-F''_\tau$ or $-K'_a$ decreases to approximately 0 at increasingly higher flows ($Re >> 1$). The critical hydraulic gradient i at which $-F''_\tau$ or $-K'_a$ decreases to approximately 0 is approximately 1 for all diverging converging pores, although they have different β. The decrease in $-F''_\tau$ or $-K'_a$ to approximately 0 indicate that growth in eddies ceases and there are no more variations in K or K_a. The growth in eddies is limited by the pore dimensions and the pressure (normal force) in the bulk flow region. From $Re >> 1$ flow conditions onward, the bulk flow gets limited to a pipelike flow channel (Figure 2f), and the $q(i)$ functional form once again follows Darcy's law.

[57] We found that the pore geometry as characterized by β plays a vital role in controlling the nonlinear characteristics of Forchheimer flows. By using the concept of β, we can rank the significance of using Forchheimer relationships for various cases. The controls on Forchheimer flow characteristics discussed here will also assist in further theoretical development of Forchheimer laws.

3.9. Forces Controlling Apparent Hydraulic Conductivity K_a

[58] In the previous section, we noticed a systematic decreasing behavior in K_a that varied for different pore geometries. Here we examined the role of different resistive forces in controlling the variations in K_a. Similar to sections 3.5 and 3.6, we examined the total drag (F_D), its components, the friction drag (F_τ), and the form drag (F_N) from the pore walls of three different diverging-converging pores with β values of 6.9, 8.5, and 12.5. We also examined the evolution in $f_{\tau,z}$ distribution on the pore walls as the flows become non-Darcy and when eddies grow to occupy an increasingly larger pore volume at increasing Re flows.

[59] In examining the total drag F_D during $Re > 1$ flows, we once again found that it does not control even K_a of pores. In comparison with variations in K_a, F_D is the same and shows a similar rate of linear increase as flows increase from $Re \sim 0$ to $Re >> 1$ (Figure 6a). During non-Darcy flows, the rate of increase in F_τ with increasing i decreases, and the rate of increase in F_N with increasing i increases (Figure 6b), such that at all flow conditions, $F_N + F_\tau = F_D$. The increase in the rate of increase in F_N eventually leads to flows where $F_N > F_\tau$ (Figure 6b); however, the decrease in K_a is not accompanied by any variation related to transition of F_N becoming the dominant resistive force. At $Re >> 1$ flows, if F_N controlled K_a, a larger F_N should

correspond to smaller K_a (just like the relationship between F_τ and K for the Darcy flow regime); however, we observed the opposite. We found that the examination of the friction drag and the form drag offered no clear insight about their control on K_a.

[60] We further examined the evolution in $f_{\tau,z}$ distribution on the walls of diverging-converging pores with β values of 6.9, 8.5, 12.5, and 24 (Figure 7) to see if it offers any additional insight on the controls on K_a. As the flow conditions increase from $Re \sim 0$ to $Re >> 1$, the distribution of $f_{\tau,z}$ shows reversal in the direction of friction drag in major part of pore domains (Figures 7b–7e), which is due to growth in eddies, and the counter flow contributes to the reversal in the direction of friction drag. However, as the flow conditions increase from $Re \sim 0$ to $Re >> 1$, the distribution of $f_{\tau,z}$ near pore throats show no distinct differences in any pore (Figures 7b–7e). The part of pore boundaries facing the bulk flow receives up to twice the $f_{\tau,z}$ relative to the opposite side of pores (Figure 7e). With increasing flows, the boundary area with $+f_{\tau,z}$ increases, whereas the area with $-f_{\tau,z}$ decreases. Thus, the net rate of increase in friction drag (F'_τ) decreases with increasing i (Figures 6b and 8b). Between the diverging-converging pores, the degree of boundary stress modification (boundary area subjected to flow reversal) and the magnitude of localized stress around flow separations are the highest for the pore with $\beta = 6.9$ and the lowest for pore with $\beta = 12.5$. In comparison, the pipe domain has a uniform stress distribution across all flow conditions. The diverging-converging pore geometry and eddies therein contribute to a large variability in the distribution of boundary stresses and the intensity of localized stresses, which results due to flow separations. However, there is no distinct pattern regarding how the drag forces control K_a.

[61] As an explanation for the decrease in K_a during Forchheimer flows, we consider our previous finding that the decrease in K_a is due to an increase in the size of eddies inside pores that reduces the average diameter of the advective flow channel. *Chaudhary et al*. [2011] have quantified the ratio of the pore volume occupied by eddies to the total pore volume (ε) from viscous to inertial flow regimes in a tortuous pore. This dimensionless ratio ε is found to be inversely related to K_a [*Chaudhary et al*., 2011]. The increase in ε signifies a decrease in the radius of advective flow channel, and the decrease in K_a can be explained by using Hagen-Poiseuille's law, in which the "hydraulic conductivity" of an idealized cylindrical pipe is nonlinearly related to the pore radius via $K \sim R^2$. However, in the geometry of advective flow channel, its boundary is modified due to the presence of an eddy and the pipe flow follows no-slip conditions; therefore, a variation from the $K_a \sim R^2$ sensitivity is expected. At flow conditions ($Re >> 1$) around the maximum decrease in the radius of the advective flow channel, the size or the radius of advective flow channel approaches similar values in all pores, which results in convergence of K_a to similar values. Therefore, the effect of shrinking of advective flow channel due to physical growth in eddy K_a seems to overwhelm any effects due to dominance of form drag, which would also decrease K_a. This is what we observed between our model diverging-converging pores (Figure 8a).

4. Summary and Conclusions

a. We analyzed and compared fluid flow characteristics and hydraulic properties of several pores with systematic variation in their diverging-converging geometry and used the uniform pipe as an end member. The geometries of all pores that also include the pipe are constrained by a nondimensional hydraulic shape factor β. We found that the hydraulic conductivity K of pores, including the pipe, is inversely proportional to β with a power of 3/2. This power-law relationship is similar in form to *Kozeny*'s [1927] equation for capillaries, where he inversely related K to "specific surface" M with a power of 2.

b. At $Re \sim 0$ laminar flow conditions, viscous eddies exist in all diverging-converging pores, except the pore with $\beta = 5.9$. In comparison, the pipe domain ($\beta = 24$) does not have viscous eddies. Viscous eddies, although present at $Re \sim 0$ flow conditions, do not influence the Darcy relationship. β shows no control in the size or location of viscous eddies. Eddy size is dependent on how close grain boundaries are to each other, i.e., the wedging of grain boundaries around the no-flow pore throats.

c. The diverging-converging pores contribute to a broader distribution of velocities relative to the pipe. Velocity distributions have an inverse pattern between the diverging-converging pores and the pipe. The pipe flow is dominated by high velocities, whereas the diverging-converging pores are dominated by low velocities. The magnitude of velocity and the spread in its distribution are inversely related with β. These differences between pores are the largest during viscous flows and progressively become smaller as the flows gradually become inertial.

d. The growth in viscous eddies at $Re \sim 1$ leads to the failure of Darcy's law in all diverging-converging pores. In comparison, Darcy's law does not fail in the pipe domain ($\beta = 24$). There exists an increasing trend between the critical flow conditions (i or Re) at which Darcy's law fails and β. For example, Darcy's law fails in pores with $\beta = 12.5$ and $\beta = 16$ at hydraulic gradient $i = 0.016$ or $Re = 1$ and $i = 0.025$ or $Re = 1.6$, respectively. However, no distinct relationship between the pore β and the critical i, at which K becomes nonlinear, is established. As β decreases, the magnitude of vorticity increases. The higher vorticities in pores with smaller β increase the propensity of viscous eddies to grow and consequently promote Darcy's law to fail at increasing flow velocities.

e. Of all resistive forces that may control K during Darcy flows, we found that the friction drag F_τ is the dominant force that contributes to the differences in K. For example, a pore with a high F_τ corresponds to having a low K and vice versa. The total drag force F_D is the same for all pores and does not explain for the differences in K. The form drag F_N is either nil or negligible in comparison with F_τ. Between different pores, the differences in K or F_τ of a pore are associated with the distribution of local friction drag $f_{\tau,z}$ on the pore boundary. The pore geometry controls the relative proportion of the wall that is located at and near pore throats. Most of the resistance

(viscous dissipation) offered by the pore occurs at the pore throats. Thus, a pore with a larger boundary near pore throats (e.g., $\beta = 16$) offers a larger resistance to flow and results in a lower K relative to a pore with a smaller boundary area near pore throats (e.g., $\beta = 12.5$). In other words, the differences in pore K are largely due to the differences in pore geometry near pore throats.

f. Forchheimer relationship describes the nonlinearity in Darcy's law, i.e., $i \propto q^m$. In all diverging-converging pores, the $i \propto q^m$ relationship follows a quadratic function with $R^2 = 0.99$ and a cubic function with $R^2 = 1$. In comparison, the pipe flow follows the $i \propto q^1$ relationship. Forchheimer flow characteristics define a systematic decrease in K_a, which is a result of eddy growth behavior at increasing flow conditions. The systematic decrease in K_a at $Re > 1$ flow conditions initially has a large rate of decrease in K_a, and later at $Re >> 1$, the rate of decrease in K_a approaches approximately 0, and the $q(i)$ functional form once again follows Darcy-type relationship.

g. At $Re > 1$ flows, the degree of nonlinearity in the $q(i)$ functional form is inversely related to β. The degree of nonlinearity in $q(i)$ or how much decrease in K_a occurs at increasing flow conditions is the highest in a pore with the smallest $\beta = 5.6$ and becomes smaller and smaller as β approaches that of the pipe ($\beta = 24$). Further and expectedly, there is no nonlinearity in $q(i)$ relationship in the pipe flow. Darcy's law stays valid in the pipe domain, as long as flow is laminar.

h. During Forchheimer flows ($Re > 1$), the total drag F_D or its components, the friction drag F_τ, and the form drag F_N offer no insight about variations in the apparent hydraulic conductivity K_a. Instead, we argued that the decrease in K_a at increasing flow conditions is primarily due to an increase in the size of eddies that decreases the advective pore volume.

i. Modifications in the fluid flow field due to diverging-converging pore geometries are significant. The pipe domain, which mimics a capillary tube model or a simple pore-network model, does not capture any of the effects described here from the diverging-converging pores. β plays a critical role in determining the modifications in fluid flow fields both during Darcy flows and Forchheimer flows. Therefore, it is very important to consider actual diverging-converging pore geometries in studying pore-level fluid dynamics. Our findings provide a foundation for further theoretical work on pore-scale to continuum-scale porous media flows from viscous to inertial regimes.

[62] **Acknowledgments.** This work is supported as part of the Center for Frontiers of Subsurface Energy Security (CFSES) at the University of Texas at Austin, an Energy Frontier Research Center funded by the U.S. Department of Energy, Office of Science, Office of Basic Energy Sciences under award DE-SC0001114. Additional support was provided by the Geology Foundation of the University of Texas. The authors thank the anonymous reviewers whose suggestions helped to improve the manuscript.

References

Balhoff, M., and M. F. Wheeler (2009), A predictive pore-scale model for non-Darcy flow in porous media, *SPE J.*, *14*(4), 579–587.

Bear, J. (1972), *Dynamics of Fluids in Porous Media*, Elsevier, New York.

Bennett, P. C., F. K. Hiebert, and J. R. Rogers (2000), Microbial control of mineral-groundwater equilibria: Macroscale to microscale, *Hydrogeol. J.*, *8*(1), 47–62, doi:10.1007/s100400050007.

Blake, S. P. (1922), The resistance of packing to fluid flow, *Trans. Am. Inst. Chem. Eng.*, *14*, 415.

Blunt, M. J., M. D. Jackson, M. Piri, and P. H. Valvatne (2002), Detailed physics, predictive capabilities and macroscopic consequences for pore-network models of multiphase flow, *Adv. Water Resour.*, *25*(8–12), 1069–1089.

Bolster, D., M. Dentz, and T. Le Borgne (2009), Solute dispersion in channels with periodically varying apertures, *Phys. Fluids*, *21*(5), 056601–1–056601–12.

Bouquain, J., Y. Meheust, D. Bolster, and P. Davy (2012), The impact of inertial effects on solute dispersion in a channel with periodically varying aperture, *Phys. Fluids*, *24*(8), 083602, doi:10.1063/1.4747458.

Brenner, H., and P. M. Adler (1982), Dispersion resulting from flow through spatially periodic porous-media. 2. Surface and intraparticle transport, *Philos. Trans. R. Soc. Lond. Ser. A: Math. Phys. Eng. Sci.*, *307*(1498), 149–200.

Bryant, S., and M. Blunt (1992), Prediction of relative permeability in simple porous-media, *Phys. Rev. A*, *46*(4), 2004–2011.

Cao, J., and P. K. Kitanidis (1998), Adaptive finite element simulation of Stokes flow in porous media, *Adv. Water Resour.*, *22*(1), 17–31.

Cardenas, M. B. (2008), Three-dimensional vortices in single pores and their effects on transport, *Geophys. Res. Lett.*, *35*, L18402, doi:10.1029/2008GL035343.

Cardenas, M. B., D. T. Slottke, R. A. Ketcham, and J. M. Sharp (2007), Navier-Stokes flow and transport simulations using real fractures shows heavy tailing due to eddies, *Geophys. Res. Lett.*, *34*, L14404, doi:10.1029/2007GL030545.

Carman, P. C. (1938), The determination of the specific surface of powders, *J. Soc. Chem. Ind. Trans.*, *57*, 225.

Chaudhary, K., M. B. Cardenas, W. Deng, and P. Bennett (2011), The role of eddies inside pores in the transition from Darcy to Forchheimer flows, *Geophys. Res. Lett.*, *38*, L24405, doi:10.1029/2011GL050214.

Chen, Z., S. L. Lyons, and G. Qin (2001), Derivation of the Forchheimer law via homogenization, *Transp. Porous Media*, *44*(2), 325–335.

Cheng, M., and K. C. Hung (2006), Vortex structure of steady flow in a rectangular cavity, *Comput. Fluids*, *35*(10), 1046–1062.

Cheng, N. S., Z. Y. Hao, and S. K. Tan (2008), Comparison of quadratic and power law for nonlinear flow through porous media, *Exp. Thermal Fluid Sci.*, *32*(8), 1538–1547.

Chukwudozie, C. P., M. Tyagi, S. O. Sears, and C. D. White (2012), Prediction of non-Darcy coefficients for inertial flows through the castlegate sandstone using image-based modeling, *Transp. Porous Media*, *95*(3), 563–580.

Collins, W. M., and S. C. R. Dennis (1976), Viscous eddies near a 90 degrees and a 45 degrees corner in flow through a curved tube of triangular cross-section, *J. Fluid. Mech.*, *76*, 417–432.

COMSOL Multiphysics (2008), COMSOL Multiphysics Version 3.5a. [Available at: http://www.comsol.com.].

Darcy, H. P. G. (1856), *Les Fontaines Publiques de la Ville de Dijon*, Victor Dalmont, Paris.

Dykaar, B. B., and P. K. Kitanidis (1996), Macrotransport of a biologically reacting solute through porous media, *Water Resour. Res.*, *32*(2), 307–320, doi:10.1029/95WR03241.

Fourar, M., G. Radilla, R. Lenormand, and C. Moyne (2004), On the nonlinear behavior of a laminar single-phase flow through two and three-dimensional porous media, *Adv. Water Resour.*, *27*(6), 669–677.

Guglielmini, L., R. Rusconi, S. Lecuyer, and H. A. Stone (2011), Three-dimensional features in low-Reynolds-number confined corner flows, *J. Fluid. Mech.*, *668*, 33–57.

Hasimoto, H., and O. Sano (1980), Stokeslets and eddies in creeping flow, *Annu. Rev. Fluid Mech.*, *12*, 335–363.

Hassanizadeh, S. M., and W. G. Gray (1987), High-velocity flow in porous-media, *Transp. Porous Media*, *2*(6), 521–531.

Joekar-Niasar, V., M. Prodanovic, D. Wildenschild, and S. M. Hassanizadeh (2010), Network model investigation of interfacial area, capillary pressure and saturation relationships in granular porous media, *Water Resour. Res.*, *46*, W06526, doi:10.1029/2009WR008585.

Kitanidis, P. K., and B. B. Dykaar (1997), Stokes flow in a slowly varying two-dimensional periodic pore, *Transp. Porous Media*, *26*(1), 89–98, doi:10.1023/A:1006575028391.

Kozeny, J. (1927), Ueber kapillare Leitung des Wassers im Boden, *Akad. Wiss. Wien*, *132*(2A), 271–306.

Leneweit, G., and D. Auerbach (1999), Detachment phenomena in low Reynolds number flows through sinusoidally constricted tubes, *J. Fluid. Mech.*, *387*, 129–150.

Lugt, H. J. (1996), *Introduction to Vortex Theory*, Vortex Flow Press, Potomac, Md.

Ma, H., and D. W. Ruth (1993), The microscopic analysis of high Forchheimer number flow in porous-media, *Transp. Porous Media*, *13*(2), 139–160.

Ma, H., and D. W. Ruth (1994), A numerical-analysis of the interfacial drag force for fluid-flow in porous-media, *Transp. Porous Media*, *17*(1), 87–103.

Maier, R. S., D. M. Kroll, Y. E. Kutsovsky, H. T. Davis, and R. S. Bernard (1998), Simulation of flow through bead packs using the lattice Boltzmann method, *Phys. Fluids*, *10*(1), 60–74.

Maier, R. S., D. M. Kroll, H. T. Davis, and R. S. Bernard (1999), Simulation of flow in bidisperse sphere packings, *J. Colloid Interface Sci.*, *217*(2), 341–347.

Malevich, A. E., V. V. Mityushev, and P. M. Adler (2006), Stokes flow through a channel with wavy walls, *Acta Mech.*, *182*(3/4), 151–182.

Man, H. N., and X. D. Jing (1999), Network modelling of wettability and pore geometry effects on electrical resistivity and capillary pressure, *J. Pet. Sci. Eng.*, *24*(2–4), 255–267.

McClure, J. E., W. G. Gray, and C. T. Miller (2010), Beyond anisotropy: Examining non-Darcy flow in asymmetric porous media, *Transp. Porous Media*, *84*(2), 535–548.

Meleshko, V. V. (1996), Steady Stokes flow in a rectangular cavity, *Proc. R. Soc. Lond. Ser. A: Math. Phys. Eng. Sci.*, *452*(1952), 1999–2022.

Moffatt, H. K. (1964), Viscous and resistive eddies near a sharp corner, *J. Fluid. Mech.*, *18*, 1–18.

Obrien, V. (1972), Closed streamlines associated with channel flow over a cavity, *Phys. Fluids*, *15*(12), 2089–2097.

Pan, C., M. Hilpert, and C. T. Miller (2004), Lattice-Boltzmann simulation of two-phase flow in porous media, *Water Resour. Res.*, *40*, W01501, doi:10.1029/2003WR002120.

Panfilov, M., and M. Fourar (2006), Physical splitting of nonlinear effects in high-velocity stable flow through porous media, *Adv. Water Resour.*, *29*(1), 30–41, doi:10.1016/j.advwatres.2005.05.002.

Pozrikidis, C. (1987), Creeping flow in two-dimensional channels, *J. Fluid. Mech.*, *180*, 495–514.

Rothman, D. H. (1988), Cellular-automaton fluids—A model for flow in porous-media, *Geophysics*, *53*(4), 509–518.

Saeger, R. B., L. E. Scriven, and H. T. Davis (1991), Flow, conduction, and a characteristic length in periodic bicontinuous porous-media, *Phys. Rev. A*, *44*(8), 5087–5090.

Saeger, R. B., L. E. Scriven, and H. T. Davis (1995), Transport processes in periodic porous-media, *J. Fluid. Mech.*, *299*, 1–15.

Shen, C., and J. M. Floryan (1985), Low Reynolds-number flow over cavities, *Phys. Fluids*, *28*(11), 3191–3202.

Sisavath, S., X. D. Jing, and R. W. Zimmerman (2001), Creeping flow through a pipe of varying radius, *Phys. Fluids*, *13*(10), 2762–2772.

Skjetne, E., and J. L. Auriault (1999), New insights on steady, non-linear flow in porous media, *Eur. J. Mech. B: Fluids*, *18*(1), 131–145.

Taneda, S. (1979), Visualization of separating Stokes flows, *J. Phys. Soc. Jpn.*, *46*(6), 1935–1942.

Valvatne, P. H., M. Piri, X. Lopez, and M. J. Blunt (2005), Predictive pore-scale modeling of single and multiphase flow, *Transp. Porous Media*, *58*(1/2), 23–41, doi:10.1007/s11242–004-5468–2.

Yoon, H., A. J. Valocchi, C. J. Werth, and T. Dewers (2012), Pore-scale simulation of mixing-induced calcium carbonate precipitation and dissolution in a microfluidic pore network, *Water Resour. Res.*, *48*, W02524, doi:10.1029/2011WR011192.